AIP Advances

Magnetotransport in Bi_2Se_3 thin films epitaxially grown on Ge(111)

Cite as: AIP Advances **8**, 115125 (2018); https://doi.org/10.1063/1.5048547
Submitted: 16 July 2018 . Accepted: 08 November 2018 . Published Online: 21 November 2018

T. Guillet, A. Marty, C. Beigné, C. Vergnaud, M.-T. Dau, P. Noël, J. Frigerio, G. Isella, and M. Jamet

ARTICLES YOU MAY BE INTERESTED IN

Linear positive and negative magnetoresistance in topological insulator Bi_2Se_3 flakes
Applied Physics Letters **113**, 113503 (2018); https://doi.org/10.1063/1.5044686

The quantum spin Hall effect and topological insulators
Physics Today **63**, 33 (2010); https://doi.org/10.1063/1.3293411

Confined-path interference suppressed quantum correction on weak antilocalization effect in a $BiSbTeSe_2$ topological insulator
Applied Physics Letters **112**, 032102 (2018); https://doi.org/10.1063/1.5009507

© 2018 Author(s).

AIP ADVANCES **8**, 115125 (2018)

Magnetotransport in Bi_2Se_3 thin films epitaxially grown on Ge(111)

T. Guillet,[1] A. Marty,[1] C. Beigné,[1] C. Vergnaud,[1] M.-T. Dau,[1] P. Noël,[1] J. Frigerio,[2] G. Isella,[2] and M. Jamet[1,a]

[1]*Univ. Grenoble Alpes, CEA, CNRS, Grenoble INP (Institute of Engineering Univ. Grenoble Alpes), INAC-Spintec, 38000 Grenoble, France*

[2]*LNESS-Dipartimento di Fisica, Politecnico di Milano, Polo di Como, via Anzani 42, 22100 Como, Italy*

(Received 16 July 2018; accepted 8 November 2018; published online 21 November 2018)

Topological insulators (TIs) like Bi_2Se_3 are a class of material with topologically protected surface states in which spin-momentum locking may enable spin-polarized and defect-tolerant transport. In this work, we achieved the epitaxial growth of Bi_2Se_3 thin films on germanium, which is a key material for microelectronics. Germanium also exhibits interesting properties with respect to the electron spin such as a spin diffusion length of several micrometers at room temperature. By growing Bi_2Se_3 on germanium, we aim at combining the long spin diffusion length of Ge with the spin-momentum locking at the surface of Bi_2Se_3. We first performed a thorough structural analysis of Bi_2Se_3 films using electron and x-ray diffraction as well as atomic force microscopy. Then, magnetotransport measurements at low temperature showed the signature of weak antilocalization as a result of two-dimensional transport in the presence of spin-orbit coupling. We interpret our results as the signature of magnetotransport in a single strongly coupled coherent channel in the presence of surface to bulk scattering. Interestingly, the magnetotransport measurements also point out that the conduction channel can be tuned between the Bi_2Se_3 film and the Ge layer underneath by means of the bias voltage or the applied magnetic field. This result suggests that the Bi_2Se_3/Ge junction is a promising candidate for tuning spin-related phenomena at interfaces between TIs and semiconductors. © *2018 Author(s). All article content, except where otherwise noted, is licensed under a Creative Commons Attribution (CC BY) license (http://creativecommons.org/licenses/by/4.0/).* https://doi.org/10.1063/1.5048547

I. INTRODUCTION

In the past decade, topological insulators (TI) have gained much interest in the field of spintronics for the generation and detection of spin currents. Three-dimensional (3D) TI are predicted to exhibit original properties like topologically protected surface states (TSS) showing Dirac band dispersion and strong spin-momentum locking.[1,2] The existence of these states was rapidly confirmed by angle-resolved photoemission spectroscopy (ARPES)[3] on films grown by molecular beam epitaxy (MBE). Since then, the growth and transport properties of bismuth-based compounds such as Bi_2Se_3 and Bi_2Te_3[4–6] were extensively studied both experimentally[7–12] and theoretically.[13–15] In particular, the existence of topologically protected surface states could be demonstrated through their signature in magnetotransport experiments. Following the predictions of two-dimensional transport, quantum corrections to the conductivity are expected and low temperature magnetoresistance measurements exhibit weak (anti)localization (WL and WAL).[16] Furthermore, the surface states exhibit a helical spin texture due to strong spin-momentum locking. Hence, a charge current flowing into the surface states is spin-polarized. The epitaxial growth of TI on conventional semiconductors appears as a very promising route to develop original spintronic devices by coupling spin generation in TSS at

[a]Electronic address: matthieu.jamet@cea.fr

 © Author(s) 2018

the interface with a long spin diffusion length (l_{sf}) material that can also be optically active like germanium.[17,18] In this study, we report the epitaxial growth of a Bi_2Se_3 thin film by MBE on low-doped Ge(111) ($p \approx 10^{15}$ cm^{-3}). Magnetoresistance measurements at low temperature clearly show the two-dimensional transport in a single coherent channel corresponding to strongly coupled surfaces and bulk states. Since the film is *n*-doped by growth-induced selenium vacancies, we demonstrate the existence of a *pn* junction that can exhibit two transport regimes depending on the bias voltage and magnetic field applied to the junction. By adjusting both parameters, it is possible to select the Bi_2Se_3 channel with spin-momentum locking at surface states or the Ge channel with long spin diffusion length.

II. SAMPLE GROWTH

Ultrathin films of Bi_2Se_3 were grown on Ge(111) by MBE, the surface quality and structure were followed by reflection high-energy electron diffraction (RHEED) all along the growth. Before the growth of Bi_2Se_3, the Ge(111) surface was first annealed up to 850°C under ultrahigh vacuum (UHV) ($p \approx 5 \times 10^{-10}$ mbar) in order the remove the native germanium oxide. Then, we used soft argon etching and performed a subsequent annealing to obtain the Ge (2×8) surface reconstruction as shown in Fig. 1a and 1b. In order to initiate the epitaxial growth of Bi_2Se_3, we first deposited one monolayer (ML) of Bi at room temperature (see Fig. 1c and 1d) and annealed the substrate until the Bi/Ge(111)-($\sqrt{3} \times \sqrt{3}$)R30° surface reconstruction appeared as shown in Fig. 1e and 1f. This Bi layer prevents the reaction of Ge with Se to form GeSe alloys.[6] Bi_2Se_3 was then grown by co-depositing Bi and Se at a substrate temperature of 220°C. Bi and Se were evaporated using an e-beam evaporator and a Knudsen cell operating at ≈ 200°C, respectively. Bi and Se evaporation rates were adjusted in order to reach a high Se:Bi ratio of about 15:1 and limit the presence of Se vacancies in the film. Fig. 1g and 1h show characteristic RHEED patterns along two different azimuths of the as-grown 12 quintuple layers (QL) of Bi_2Se_3. They exhibit a slight three-dimensional modulation as a consequence of the surface roughness as shown by atomic force microscopy (AFM) in the following. 1 QL corresponds to 1 nm. The lamellar crystal structure is schematically shown in Fig. 1i. We selected this Bi_2Se_3 film thickness because thicknesses above 6 QL are required to obtain a 3D topological insulator behavior with gapless surface states. As seen by means of ARPES in Ref. 19, for thicknesses > 6 QL, the

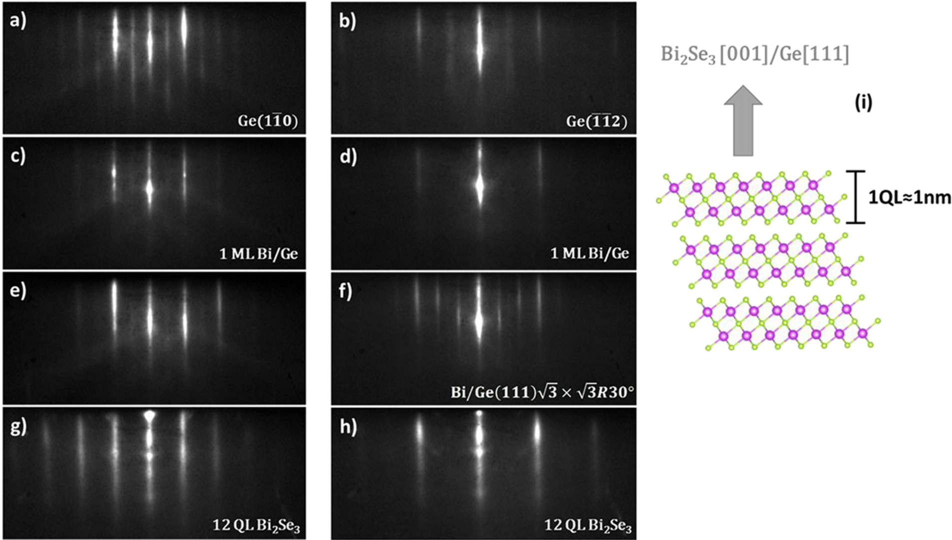

FIG. 1. RHEED patterns recorded during the growth of Bi_2Se_3 on Ge(111). (a), (b) Bare Ge(2×8) reconstructed surface after ion bombardment and annealing up to 850°C. (c), (d) After deposition of one monolayer of Bi at room temperature. (e), (f) Bi/Ge(111)-($\sqrt{3} \times \sqrt{3}$)R30° surface reconstruction after annealing at 500°C during 10 minutes. (g), (h) 12 QL of Bi_2Se_3 grown at 220°C. (i) Quintuple layer structure of Bi_2Se_3.

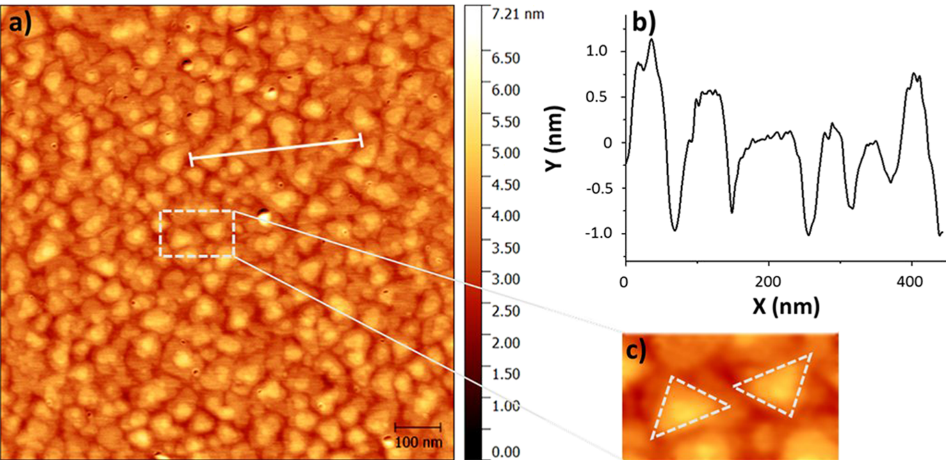

FIG. 2. (a) Atomic force microscopy image of the 12 QL-thick Bi_2Se_3 film. (b) Height profile along the light grey solid line shown in (a). (c) Zoom-in of the AFM image showing two triangular grains pointing at opposite directions.

Dirac-cone-like band structure of surface states starts to form with an increased spin polarization of the topological surface electrons. Furthermore, for thicknesses > 6 QL, an increased contribution of the surface states to electrical transport is obtained as shown in Ref. 20 and 21. In particular, the main feature that can be captured in magnetotransport measurements is a crossover from a unitary behavior or weak localization to weak anti-localization when the thickness of the film increases, this is due to a gap opening in the TSS for thicknesses < 6 QL. For thicker films (> 20 QL), an increased bulk contribution is expected to reduce the TSS contribution to electrical conduction. Hence, for a 12 QL-thick Bi_2Se_3 film, the TSS are expected to be gapless and the bulk contribution to magnetotransport to be small.

A characteristic AFM image in Fig. 2a shows the film morphology. Typical steps of 1-2 QL height can be seen on the profile shown in Fig. 2b. The root-mean-square roughness is of the order of 0.51 nm. The film is capped with 2 nm of aluminum to prevent from oxidation and pollution. The aluminum layer is grown in two steps: 1 nm was deposited by e-beam evaporation and 1 nm by magnetron sputtering in the same UHV setup. The final RHEED pattern exhibits rings characteristic of a polycrystalline Al layer.

III. STRUCTURAL CHARACTERIZATION

In-plane and out-of-plane x-ray diffraction (XRD) measurements were performed with two different diffractometers. The grazing incidence X-ray diffraction (GIXD) was done with a SmartLab Rigaku diffractometer equipped with a copper rotating anode beam tube (K_α=1.54 Å) operating at 45 kV and 200 mA. Parallel in-plane collimators of 0.5° of resolution were used both on the source and detector sides. The out-of-plane diffraction was performed using a Panalytical Empyrean diffractometer equipped with a cobalt source, (K_α=1.79 Å) operated at 35 kV and 50 mA. The incident beam divergence slit was set at 0.125° and the diffracted beam was measured using a camera PIXcel-3D detector allowing a resolution of 0.02° per pixel. Both diffractometers are equipped with multilayer mirrors on the incident beam and K_β filter on the diffracted beam.

Fig. 3a shows the symmetric out-of-plane $\theta/2\theta$ diffraction spectra along the Ge($h\ h\ h$) reciprocal direction. In addition to the substrate Ge(111) peak, the 5 other peaks can be attributed to the rhombohedral structure $R\bar{3}m$ of Bi_2Se_3.[22] They are indexed in the hexagonal unit cell (a=0.4143 nm and c=2.8636 nm) which consists of three Se-Bi-Se-Bi-Se quintuple layers separated from each other by a van der Waals gap. The relative intensities of the peaks are consistent with the calculated structure factors. It can be noticed that the 2 most intense peaks in this reciprocal direction can be easily understood: the (0015) reflection corresponds to the average lattice spacing c/15 of the 15 atomic planes regardless the nature of the atoms, whereas the (006) reflection is attributed

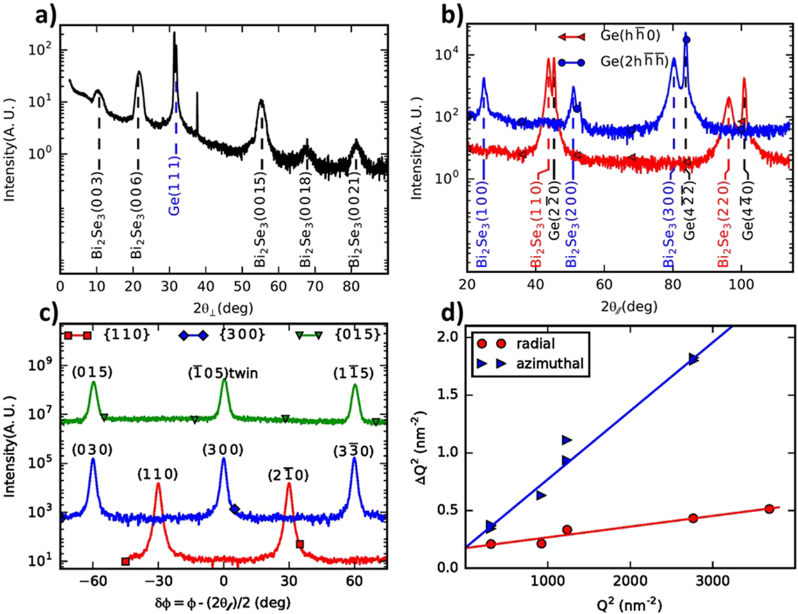

FIG. 3. (a) Out-of-plane symmetric $\theta/2\theta$ spectrum close to the substrate reciprocal direction Ge($h\ h\ h$) substrate. A small offset $\delta\omega = \omega - \theta = 0.25°$ was used to attenuate the substrate peaks and reduce the contribution from parasitic peaks (K_β, $\lambda/2\ldots$) still present despite the K_β filtering. (b) In-plane GIXD radial scans along the two reciprocal directions separated from each other by 30°: Ge($h\,\bar{h}\,0$) and Ge($2h\,\bar{h}\,\bar{h}$). The incidence angle was optimized to 0.32°. (c) In-plane GIXD azimuthal scans for two peaks families {300} and {110}. The spectra of {100}, {200} and {220} families were also measured but not shown here for clarity. The azimuthal scan of the {015} reflection shows the presence of twin domains. This measurement was performed using the same grazing incidence, 0.32°, but with suitable exit angles. (d) Square of the FWHM of Bragg peaks (in Q units) as a function of the square of the momentum transfer Q for both in-plane radial and azimuthal scans. The two linear fits show equal intercepts at the origin giving an estimation of the domains size: $D \approx 15$ nm.

to the average lattice spacing separating the 6 Bi atomic layers, Bi having the larger diffusion factor.

Figures 3b and 3c show GIXD measured with an optimized incidence angle of 0.32°. Radial scans (Fig. 3b) along the two 30° apart in-plane directions Ge($2h\,\bar{h}\,\bar{h}$) and Ge($h\,\bar{h}\,0$) give the epitaxial relationship between Bi_2Se_3 and the Ge substrate: Bi_2Se_3(110)||Ge(1$\bar{1}$0). The peak positions corresponding to the ones of bulk Bi_2Se_3 show that there is no substrate induced in-plane strain. Azimuthal scans around the Bi_2Se_3(hk0) Bragg peaks (Fig. 3c) show the in-plane alignment of Bi_2Se_3 and Ge crystals: 30° rotational domains are completely absent. However, pure in-plane measurements cannot exclude twinning which generally occurs due to the simultaneous nucleation of twinned domains on lattice mismatched substrates.[23] Indeed, the ABCAB and ACBAC stackings of the quintuple layer structure give in-plane diffraction peaks {hk0} at the same positions. Nevertheless, the 3-fold symmetry of the out-of-plane {015} reflexions allows to quantify the degree of twinning.[24] The measurement shows that the film is composed of both twins in equal proportions which leads to the presence of triangular grains pointing at opposite directions as shown in Fig. 2c.

From the Bragg peaks width in radial and azimuthal scans as a function of the momentum transfer: $Q = \frac{4\pi}{\lambda}\sin(\theta)$, we can estimate the in-plane domain size D, the in-plane mosaicity $\Delta\xi$ and the lattice parameter distribution, $\Delta a/a$ according to the quadratic relations:[25]

$$\Delta Q^2_{rad} = \left(\frac{2\pi}{D}\right)^2 + Q^2\left(\frac{\Delta a}{a}\right)^2 \tag{1}$$

$$\Delta Q^2_{azi} = \left(\frac{2\pi}{D}\right)^2 + Q^2\Delta\xi^2 \tag{2}$$

where the radial and azimuthal full width at half maximum (FWHM) in Q units are related to the diffraction peaks widths through the relations: $\Delta Q_{rad} = \frac{4\pi}{\lambda}\cos(\theta)\frac{\Delta(2\theta)}{2}$ and $\Delta Q_{azi} = Q\Delta\Phi$.

Both least-squares fits in Fig. 3d give similar domain sizes close to D=15 nm which is a lower bound since we did not consider here the setup resolution. The slopes of the fits give a lattice parameter dispersion less than 1 % (radial) and an in-plane mosaicity of $\Delta\xi$=1.4° (azimuthal) which are rather low values considering the presence of twinned domains.[24] Despite their weak intensity, the presence of forbidden peaks like (100) and (200) of Bi_2Se_3 in the radial scan of Fig. 3b comes from the non-integer number of unit cells in crystal grains. This can be due to a non-uniform layer thickness (12±1 QL), surface roughness and a substantial twin boundaries density. The absence of thickness fringes around Bragg peaks in the out-of-plane measurements (Fig. 3a) can also be explained by the film roughness shown in the AFM image of Fig. 2a.

IV. MAGNETOTRANSPORT

As-grown Bi_2Se_3 films were patterned into micron-sized Hall bars (dimensions: length L=130 μm and width W=10 μm) as shown in Fig. 4a to perform magnetoresistance (MR) and Hall measurements. The microfabrication of Hall bars required three successive steps: laser lithography to define the pattern, e-beam evaporation of Au(90 nm)/Ti(5 nm) ohmic contacts and ion beam etching. MR and Hall measurements were performed in a helium closed cycle cryostat working in the 1.6-295 K temperature range and equipped with a superconducting magnet delivering up to 7 Tesla. Fig. 4b and 4c show current-voltage ($I(V)$) curves recorded between the two extreme current leads at 1.6 K and 295 K respectively. The maximum applied current is 50 μA. We clearly see the rectification effect at the Bi_2Se_3/Ge interface at low temperature. Part of the current is shunted into Ge for $U_{xx} \geqslant 0.2$ V. For $U_{xx} < 0.2$ V, the linear behavior indicates the ohmic character of the Ti/Au contacts on Bi_2Se_3. The red curve in Fig. 4d shows the temperature dependence of the DC 4-probe longitudinal resistance R_{xx}=U_{xx}/I for an applied current of 10 μA. We find an overall semiconducting character due to the current shunting into the Ge substrate. However, the resistance saturation at low temperature shown in the inset of Fig. 4d corresponds to electrical transport into the Bi_2Se_3 film due to the increasingly high resistance of the Ge substrate and Bi_2Se_3/Ge contacts below 10 K as shown in Fig. 4b. As a comparison, we show in Fig. 4d (black curve) the temperature dependence of the Ge substrate resistance. As shown in Fig. 4a and in the following, the current shunting into the Ge substrate can be restored at low temperatures by applying larger current *i.e.* larger bias voltages. Fig. 5a and 5b show MR and Hall measurements recorded at 1.6 K with an applied current of 1 μA. R_{xx} clearly exhibits a MR dip at low magnetic field corresponding to WAL. The linear dependence of R_{xy} on the magnetic field is interpreted in terms of a single-carrier electrical transport. From the slope, we obtain a n-type doping as expected for MBE-grown Bi_2Se_3 films where Se vacancies act as donors. We find a carrier

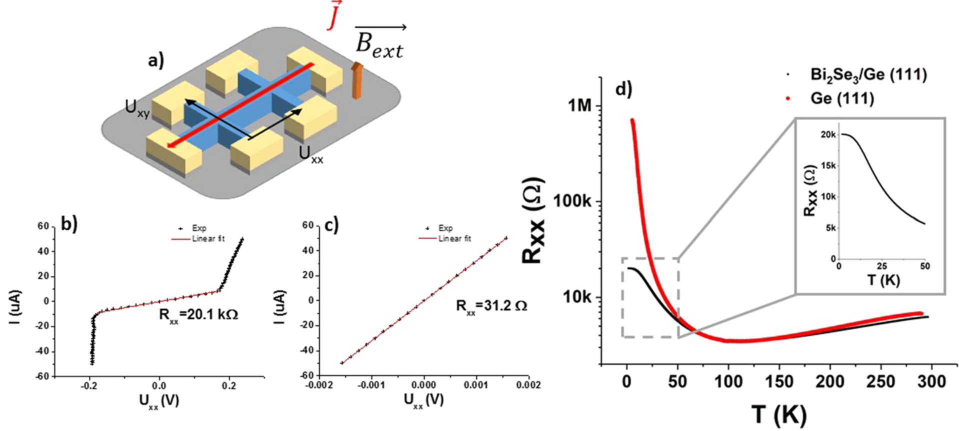

FIG. 4. (a) Sketch of the Hall bar microstructure and description of the 4-probe measurements geometry. (b), (c) $I(V)$ curves recorded between the two extreme current leads at 1.6 K and 295 K respectively. (d) Log-scale representation of the longitudinal resistance R_{xx} as a function of temperature, the red curve is for Bi_2Se_3/Ge (111) and the black curve for the substrate. Inset: zoom-in at low temperature showing the resistance saturation.

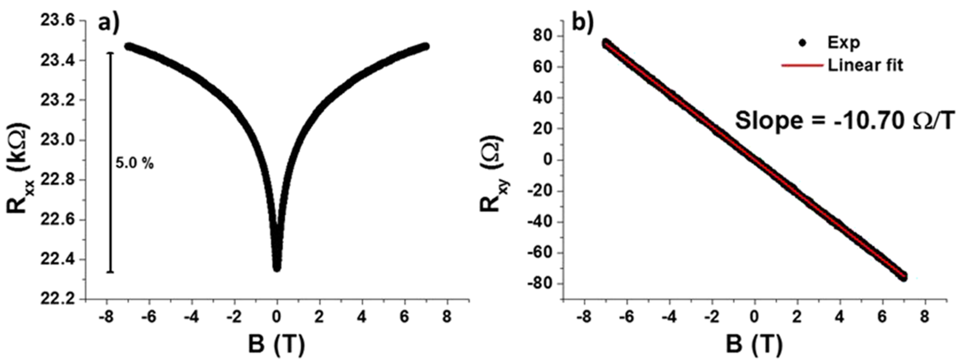

FIG. 5. (a) R_{xx} as a function of the applied magnetic field at 1.6 K. The field is perpendicular to the film. (b) Corresponding transverse Hall resistance R_{xy} at 1.6K.

concentration of 4.6 $\times 10^{19}$cm^{-3} assuming 3D transport (both into surface states and the bulk) and 5.4 $\times 10^{13}$cm^{-2} if we consider 2D transport into the surface states. We further find a low mobility of 37 cm^2/(V.s) which might be explained by the high concentration of twin defects as unveiled by XRD and AFM measurements.

The observation of WAL strongly suggests a 2D electrical transport in the presence of spin-orbit coupling.[13,16] This is supported by the temperature and angular dependences of the magnetoresistance. Fig. 6a presents MR measurements as a function of the projected magnetic field $B \times \cos(\theta)$. All the curves perfectly overlap at low fields which is the signature of WAL.[26] Fig. 6b shows the film magnetoconductance at temperatures varying from 2 K to 6 K. In Fig. 6c, the data are fitted using the Hikami-Larkin-Nagaoka (HLN) two-dimensional quantum diffusion model:[8,10,16]

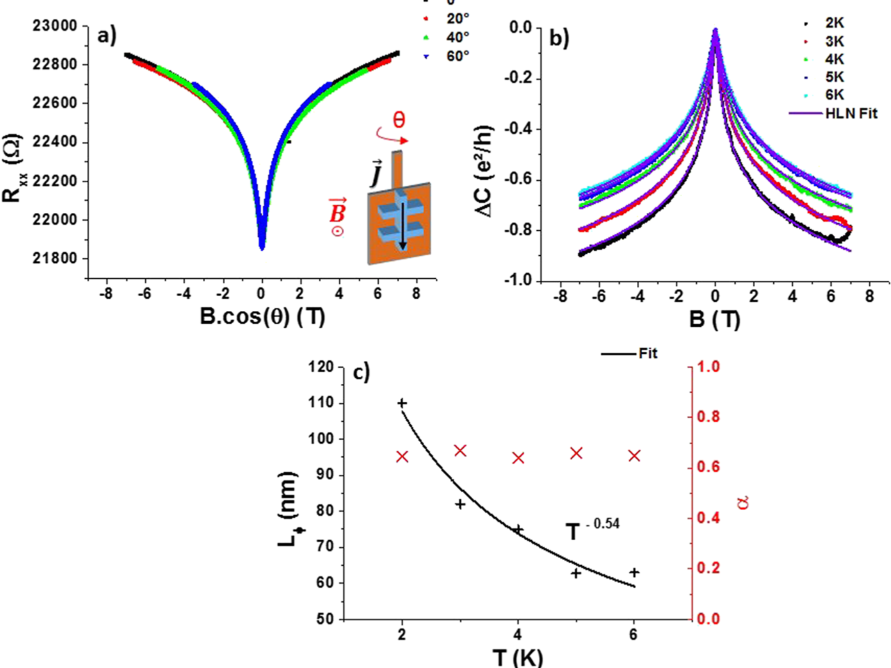

FIG. 6. (a) R_{xx} as a function of $B \times \cos(\theta)$. The angle θ is shown in the inset and defined as the angle between the surface normal and the applied magnetic field. (b) Magnetoconductance ΔC normalized to the quantum of conductance e^2/h as a function of temperature. Red solid lines are fits using the HLN model. (c) Parameters extracted from the HLN model: L_ϕ is the effective phase coherence length and α, the characteristic parameter related to the number of transport channels.

$$\Delta C = -\frac{\alpha e^2}{2\pi^2\hbar}\left[\psi\left(\frac{\hbar}{4eBL_\phi^2}+\frac{1}{2}\right)-\ln\left(\frac{\hbar}{4eBL_\phi^2}\right)\right] \tag{3}$$

where ψ is the digamma function, B is the applied magnetic field perpendicular to the film, L_Φ is the effective phase coherence length and α a parameter related to the number of channels contributing to the transport.[27,28] $\alpha = 0.5$ is for one channel contributing to the transport and $\alpha = 1$ for two channels contributing. In the literature, α varies from 0.25 to 1 depending on the thickness,[29,30] or the film fabrication technique.[9] Using the HLN model, we can extract a temperature independent α value of 0.61. This value is close to 0.5 which corresponds to a single conducting channel. For a 12 QL-thick Bi_2Se_3 film, bulk states are quantized and we can exclude pure magnetotransport into those 2D bulk states since they should give rise to a weak localization (WL) signal as predicted by Shen *et al.*[13] Considering the high electron density extracted from Hall measurements, the Fermi energy is larger than the energy spacing between the quantized bulk states of the 12 QL-thick Bi_2Se_3 film. Hence, those bulk states are energetically accessible for electron transport and scattering (non-TI regime). As a consequence, magnetotransport and the WAL take place in a single coherent channel corresponding to strongly coupled surfaces and bulk states.[12]

We find an effective phase coherence length L_ϕ of 110 nm at 1.6 K which corresponds to a lower bound as compared to the values already published: 106-237 nm;[27] 100-600 nm;[20] 75-200 nm;[31] 100-1000 nm[32] or 15-300 nm.[33] L_ϕ decreases with increasing the temperature as $T^{-0.54}$, which is in good agreement with the theory predicting $L_\phi \propto T^{-0.50}$.

Fig. 7a shows MR measurements at higher temperatures, where the germanium conducting channel is thermally activated. In this case, we find a conventional Lorentz MR behavior where $\frac{\Delta R}{R_0} \propto (\mu B)^2$ characteristic of a 3D bulk transport. The magnitude of this MR is the one expected from the high carrier mobility in germanium (see http://www.ioffe.ru/SVA/NSM/Semicond/Ge/electric.html). Fig. 7b shows R_{xy} as a function of temperature in Hall configuration. When the temperature increases, the sign of the Hall effect changes from negative for n-type doping (Bi_2Se_3 carriers) to positive for p-type doping (Ge carriers). By measuring continuously the longitudinal resistance R_{xx} as a function of the temperature for 0 Tesla and 7 Tesla, we could extract a continuous MR curve given by:

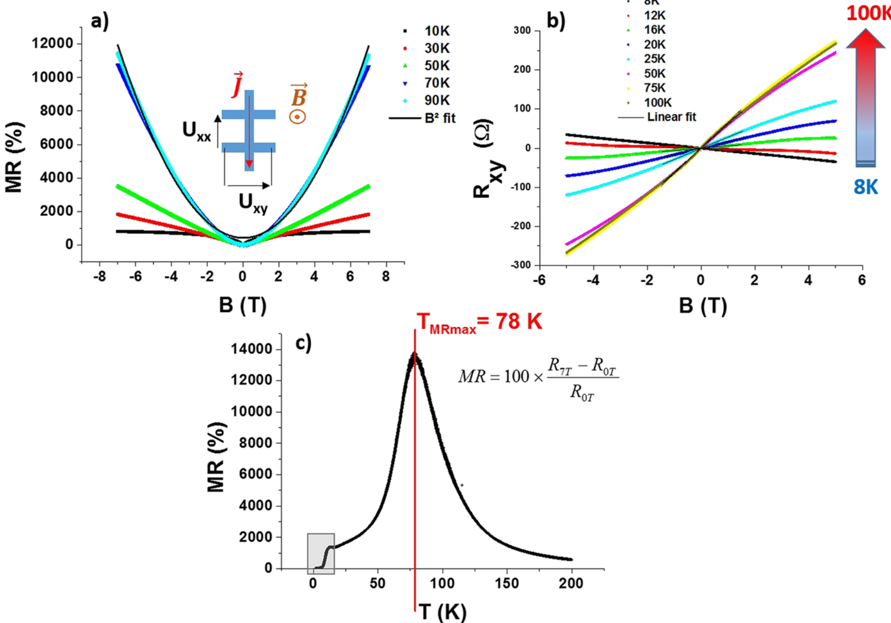

FIG. 7. (a) Longitudinal magnetoresistance measured at different temperatures. The inset shows the measurement geometry (B being perpendicular to the film). (b) Transverse resistance R_{xy} in the same geometry as a function of the temperature, the sign of the Hall effect changes as the Ge channel is being activated (c) Continuous MR(T) curve. The grey box shows the transition to magnetotransport in the Bi_2Se_3 film at low temperature.

$\frac{R_{7T}-R_{0T}}{R_{0T}}$ and shown in Fig. 7c. It shows a maximum at 78 K corresponding to the temperature at which all the dopants in Ge are thermally activated and the electron-phonon scattering is minimum. For $T \leq 10$ K, we observe a sharp drop of the MR when the charge current is no more shunted into the Ge substrate but only flows into the Bi_2Se_3 film where the MR is limited to some percents (see Fig. 5a).

Fig. 8a shows MR measurements at 1.6 K for bias currents varying from 1 μA to 50 μA. To eliminate the offset voltage due to thermal effects, the current sign is changed from $+I$ to $-I$ and the longitudinal resistance is calculated using: $R_{xx} = \frac{R_{+I}+R_{-I}}{2}$. Two different transport regimes can be observed depending on the applied magnetic field. The critical field separating those two regimes (indicated by arrows in Fig. 8a) increases with the bias current. By measuring $I(V)$ curves at different magnetic fields in Fig. 8b, we find the characteristic magnetic field dependence of a *pn*-junction $I(V)$ curve[34,35] in parallel with a resistor. The *n*-doped (resp. *p*-doped) layer can be associated to the Bi_2Se_3 film (resp. the germanium substrate). When the current is kept low enough (≈ 8 μA), the $I(V)$ curve keeps a ohmic character and the magnetotransport takes place in the Bi_2Se_3 film only. For a current higher than 8 μA, the current source generates a high enough bias voltage to make the *pn*-junction conducting and the current mostly flows into germanium. Despite its high resistivity (1 kΩ cm at 2 K), the germanium substrate is so thick (350 μm) that its resistance is much lower than the one of the Bi_2Se_3 film. This regime corresponds to the steeper slope in the $I(V)$ curve. The diode threshold voltage V_d increases with the applied magnetic field. Hence, for a given bias voltage, the magnetic field allows to select the conducting channel and magnetotransport properties. In regime 1 where the applied magnetic field is lower than a critical field (marked by a vertical arrow in Fig. 8a), the current flows in the germanium substrate and the resistance (resp. MR) is low (resp. high). In this case, the MR curve is the one of the Ge substrate that we measured independently using a second device made of pure Ge with Ti/Au ohmic contacts (not shown). In regime 2 where the applied magnetic field is higher than the critical field, the current flows in the Bi_2Se_3 film and the resistance (resp. MR) is high (resp. low). At the transition between the two regimes, we observe very sharp steps in MR curves in Fig. 8a with slopes up to 20 Ω/mT and negative differential resistances in $I(V)$ curves (Fig. 8b). These phenomena require further investigation and are out of the scope of this work.

This *pn*-junction effect at a semiconductor/topological insulator could be of great interest to tune spin transport since one can control whether the charge current is spin-polarized (regime 2) or not (regime 1). It also paves the way to develop spin-FET structures where the spin information can be transmitted by the application of an electric field. Finally, we stress the fact that we obtained the similar magnetotransport results using a 2 μm-thick epitaxial germanium film (of comparable *p*-type doping) on semi-insulating Si(111) instead of a germanium substrate. This Ge-on-Si epilayer was deposited on a 3-inch high-resistivity Si(111) wafer by low-energy plasma enhanced chemical vapor deposition at a deposition rate of ≈ 4 nm/s and a substrate temperature of 500°C.[36] Post-growth annealing cycles have been used to reduce the threading dislocation density down to $\approx 2 \times 10^7$ cm^{-2} and to improve the

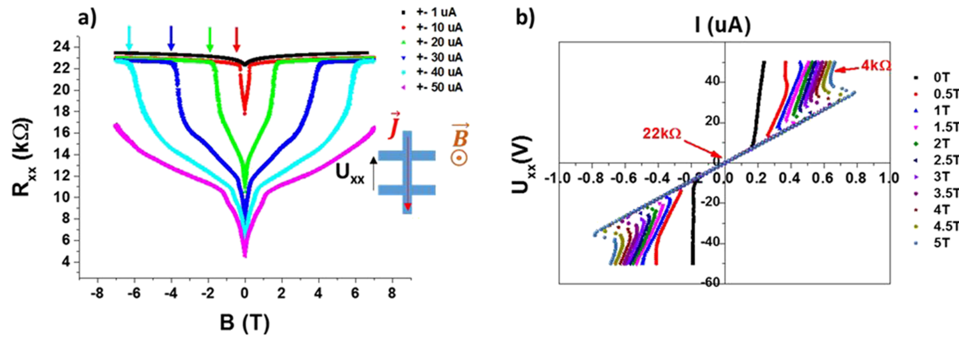

FIG. 8. (a) MR curves measured at 1.6 K for different applied currents. Two magnetotransport regimes can be clearly identified. The transition magnetic field is indicated by arrows. The inset shows the measurement geometry (B being perpendicular to the film). (b) $I(V)$ curves at different magnetic fields exhibiting a *pn*-junction behavior.

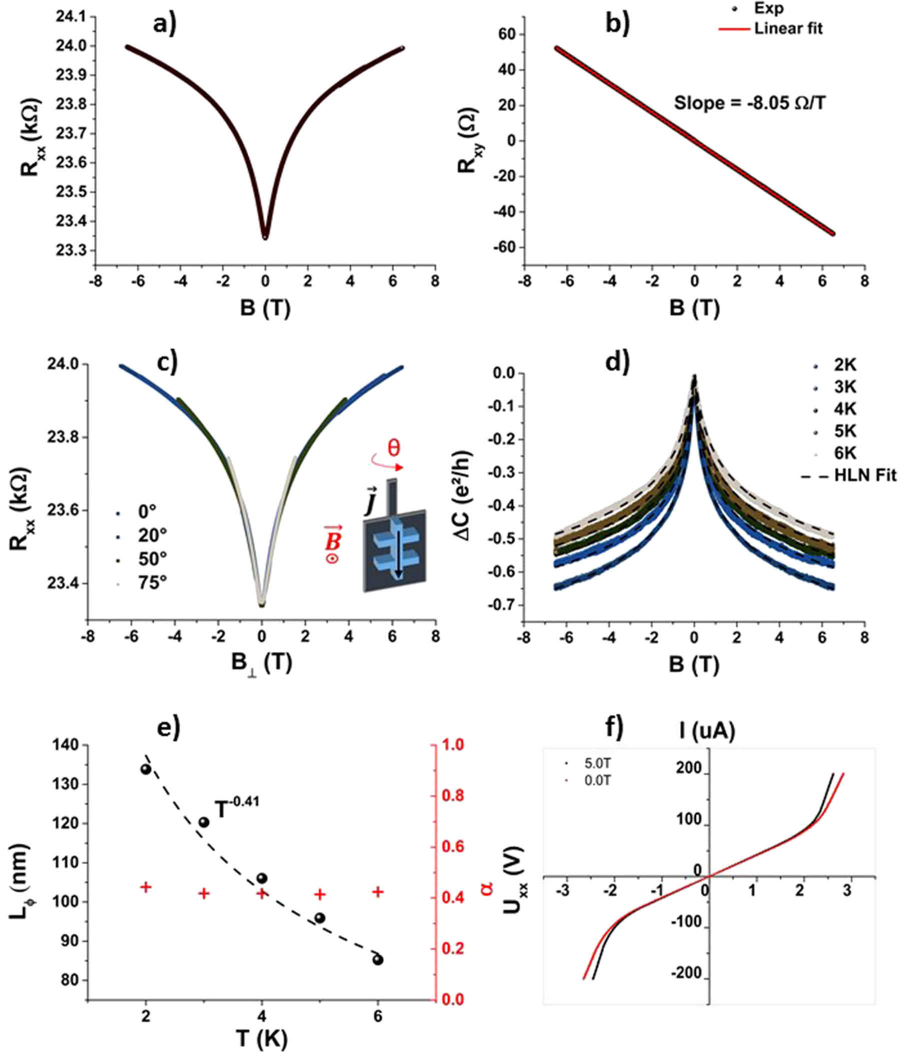

FIG. 9. Magnetotransport measurements performed on Bi_2Se_3 grown on a 2 μm-thick Ge film. (a) R_{xx} as a function of the applied magnetic field at 1.6 K. The field is perpendicular to the film. (b) Corresponding transverse Hall resistance R_{xy} at 1.6K. (c) R_{xx} as a function of $B \times \cos(\theta)$ at 1.6 K. The angle θ is defined in the inset. (d) Magnetoconductance ΔC normalized to the quantum of conductance e^2/h as a function of temperature. Black dashed lines are fits using the HLN model. (e) Parameters extracted from the HLN model: L_ϕ is the effective phase coherence length and α, the characteristic parameter related to the number of transport channels. (f) $I(V)$ curves at 0 and 5 Tesla exhibiting a *pn*-junction behavior as well as the field dependent threshold.

crystal quality.[37] All the magnetotransport results are shown in Fig. 9. At low temperature, we observe the weak anti-localization peak in the longitudinal resistance (Fig. 9a) and a linear magnetic-field dependence of the transverse resistance indicating electrical transport by a single electron population (Fig. 9b). In Fig. 9c, the resistance is plotted as a function of the magnetic field projection along the film normal $B \times \cos(\theta)$. All the curves are overlapping demonstrating a two-dimensional electrical transport. By fitting the magnetoconductance as a function of temperature using the HLN model in Fig. 9d, we derive the effective phase coherence length L_ϕ and the α parameter (Fig. 9e) which are comparable to those obtained for the Bi_2Se_3 film grown on the germanium substrate. $I(V)$ curves in Fig. 9f show the bias voltage and magnetic field dependence of the threshold between regime 1 (magnetotransport in Ge) and regime 2 (magnetotransport in Bi_2Se_3) discussed previously. Due to the much higher resistance of the 2 μm-thick Ge channel as compared to the one of the Ge wafer (by almost two orders of magnitude), the transition between regime 1 and regime 2 occurs at higher bias voltages. Similarly, the MR of the 2 μm-thick Ge film being two orders of magnitude less than the

one of the Ge substrate (due to a much lower carrier mobility), the transition between regime 1 and regime 2 occurs at higher magnetic fields.

V. CONCLUSION

In this work, we have successfully grown by epitaxy a 12 QL-thick Bi_2Se_3 film on germanium. Despite the presence of twin boundaries, we obtained a high-crystalline quality material with a surface roughness of ±1 QL. Low temperature magnetotransport measurements showed the signature of two-dimensional weak antilocalization in a single coherent channel corresponding to strongly coupled surfaces and bulk states with a phase coherence length of the order of 110 nm at 2 K. By studying the temperature dependence of the MR and Hall effect, we found that the electrical current flows into the Bi_2Se_3 film at low temperature. In this case, we measured a low MR and *n*-type doping. When the temperature increases, the electrical current is progressively shunted into the Ge layer and we measured a high MR and *p*-type doping. Finally, at 1.6 K, we could tune the conduction channel between Bi_2Se_3 and Ge by adjusting the bias voltage or the applied magnetic field. Hence, it could be possible to select electrically or magnetically the Bi_2Se_3 conduction channel with spin-momentum locking or the Ge conduction channel with a long spin diffusion length. These findings pave the way to design innovative spintronic devices by combining semiconductors and topological insulators for which the energy barrier between the two materials acts as a controllable switch between two spin transport regimes.

ACKNOWLEDGMENTS

This work was supported by the French Agence Nationale de la Recherche through the project ANR-16-CE24-0017 TOP-RISE. The LANEF framework (ANR-10-LABX-51-01) is acknowledged for its support with mutualized infrastructure. Partial support is acknowledged to the Horizon-2020 FET microSPIRE project, ID: 766955.

[1] M. Z. Hasan and C. L. Kane, Rev. Mod. Phys. **82**, 3045 (2010).
[2] H. Zhang, C.-X. Liu, X.-L. Qi, X. Dai, Z. Fang, and S.-C. Zhang, Nat. Phys. **5**, 438 (2009).
[3] D. Hsieh, Y. Xia, D. Qian, L. Wary, and M. Z. Hasan, Nature **460**, 1101 (2009).
[4] G. Zhang, H. Qin, J. Chen, X. He, L. Lu, Y. Li, and K. Wu, Adv. Func. Mat. **21**, 2351 (2011).
[5] C.-Z. Chang, K. He, L.-L. Wang, X.-C. Ma, and Q.-K. Xue, Spin **01**, 21 (2011).
[6] S. Kim, S. Lee, J. Woo, and G. Lee, Appl. Surf. Sci. **432**, 152 (2018).
[7] R. Dey, A. Roy, T. Pramanik, S. Guchhait, S. Sonde, A. Rai, L. F. Register, and S. K. Banerjee, J. Appl. Phys. **120**, 164301 (2016).
[8] H. Wang, H. Liu, C.-Z. Chang, H. Zuo, and J. Wang, Sci. Rep. **4**, 5817 (2014).
[9] W. J. Wang, K. H. Gao, and Z. Q. Li, Sci. Rep. **6**, 25291 (2016).
[10] B. Irfan, P. Bhanu, P. Joshi, A. Thamizhavel, and R. Chatterjee, Solid State Commun. **220**, 45 (2015).
[11] M. Lang, L. He, X. Kou, P. Upadhyaya, and K. L. Wang, Nano. Lett. **13**, 48 (2013).
[12] D. Kim, P. Syers, N. P. Butch, J. Paglione, and M. S. Fuhrer, Nat. Commun. **4**, 2040 (2013).
[13] H. Lu and S.-Q. Shen, Phys. Rev. B **84**, 125138 (2011).
[14] H. Lu and S.-Q. Shen, Phys. Rev. Lett. **107**, 076801 (2011).
[15] H.-Z. Lu, W.-Y. Shan, W. Yao, Q. Niu, and S.-Q. Shen, Phys. Rev. B **81**, 115407 (2010).
[16] S. Hikami, A. I. Larkin, and Y. Nagaoka, Prog. Theor. Phys. **63**, 707 (1980).
[17] M. Finazzi, F. Bottegoni, C. Zucchetti, M. Bollani, A. Ballabio, J. Frigerio, F. Rortais, C. Vergnaud, A. Marty, M. Jamet, G. Isella, and F. Ciccacci, Electronics **5**.
[18] F. Rortais, C. Vergnaud, A. Marty, L. Vila, J.-P. Attané, J. Widiez, C. Zucchetti, F. Bottegoni, H. Jaffrès, J.-M. George, and M. Jamet, Appl. Phys. Lett. **111**, 182401 (2017).
[19] M. Neupane *et al.*, Nat. Comm. **5**, 3841 (2014).
[20] A. A. Taskin, S. Sasaki, K. Segawa, and Y. Ando, Phys. Rev. Lett. **109**, 066803 (2012).
[21] N. Bansal, Y. S. Kim, M. Brahlek, E. Edrey, and S. Oh, Phys. Rev. Lett. **109**, 116804 (2012).
[22] S. Nakajima, J. Phys. Chem. Solids **24**, 479 (1963).
[23] D. Kriegner, P. Harcuba, J. Veselỳ, A. Lesnik, G. Bauer, G. Springholz, and V. Holỳ, J. Appl. Cryst. **50**, 369 (2017).
[24] F. Bonell, M. Cuxart, K. Song, R. Robles, and S. Valenzuela, Cryst. Growth Des. **17**, 4655 (2017).
[25] G. Renaud, A. Barbier, and O. Robach, Phys. Rev. B **60**, 5872 (1999).
[26] T. Chen, Q. Chen, K. Schouteden, W. Huang, and G. Wang, Nat. Comm. **5**, 5022 (2014).
[27] J. Chen *et al.*, Phys. Rev. Lett. **105**, 176602 (2010).
[28] J. Chen *et al.*, Phys. Rev. B **83**(R), 241304 (2011).
[29] Y. S. Kim, M. Brahlek, N. Bansal, E. Edrey, and S. Oh, Phys. Rev. B **84**, 073109 (2011).
[30] M. Brahlek, N. Koiorala, M. Salehi, N. Bansal, and S. Oh, Phys. Rev. Lett. **113**, 026801 (2014).
[31] M. H. Liu *et al.*, Phys. Rev. B **83**, 165440 (2011).

[32] Y. S. Kim *et al.*, Phys. Rev. B **84**, 073109 (2011).
[33] H. Steinberg, J.-B. Laloë, V. Fatemi, J. S. Moodera, and P. Jarillo-Herrero, Phys. Rev. B **84**, 233101 (2011).
[34] R. V. Aldridge, K. Davis, and M. Holloway, J. Phys. D: Appl. Phys. **8**, 64 (1975).
[35] C. Wan, X. Zhang, X. Gao, J. Wang, and X. Tan, Nature **477**, 304 (2011).
[36] E. Gatti, F. Isa, D. Chrastina, E. Müller Gubler, F. Pezzoli, E. Grilli, and G. Isella, J. Appl. Phys. **116**, 043518 (2014).
[37] J. Osmond, G. Isella, D. Chrastina, R. Kaufmann, M. Acciarri, and H. von Känel, Appl. Phys. Lett. **94**, 201106 (2009).